

ForgeDreamer: Industrial Text-to-3D Generation with Multi-Expert LoRA and Cross-View Hypergraph

Junhao Cai^{1*} Deyu Zeng^{2*} Junhao Pang¹ Lini Li¹ Zongze Wu¹ Xiaopin Zhong^{1,†}

¹Shenzhen University, Shenzhen, Guangdong 518060, China

²Guangzhou Maritime University, Guangzhou, Guangdong 510725, China

caijunhao27@gmail.com zengdeyu@gzmtu.edu.cn

{2500092013, 2500092003}@mails.szu.edu.cn {zzwu, xzhong}@szu.edu.cn

Abstract

Current text-to-3D generation methods excel in natural scenes but struggle with industrial applications due to two critical limitations: domain adaptation challenges where conventional LoRA fusion causes knowledge interference across categories, and geometric reasoning deficiencies where pairwise consistency constraints fail to capture higher-order structural dependencies essential for precision manufacturing. We propose a novel framework named ForgeDreamer addressing both challenges through two key innovations. First, we introduce a Multi-Expert LoRA Ensemble mechanism that consolidates multiple category-specific LoRA models into a unified representation, achieving superior cross-category generalization while eliminating knowledge interference. Second, building on enhanced semantic understanding, we develop a Cross-View Hypergraph Geometric Enhancement approach that captures structural dependencies spanning multiple viewpoints simultaneously. These components work synergistically improved semantic understanding, enables more effective geometric reasoning, while hypergraph modeling ensures manufacturing-level consistency. Extensive experiments on a custom industrial dataset demonstrate superior semantic generalization and enhanced geometric fidelity compared to state-of-the-art approaches. Code is available at <https://github.com/Junhaocai27/ForgeDreamer>

1. Introduction

Text-to-3D generation has emerged as a transformative technology, enabling the creation of diverse 3D content from natural language descriptions. Recent breakthroughs, led by pioneering works such as DreamFusion [32] and subsequent advances like ProlificDreamer

*Equal contribution. †Corresponding author.

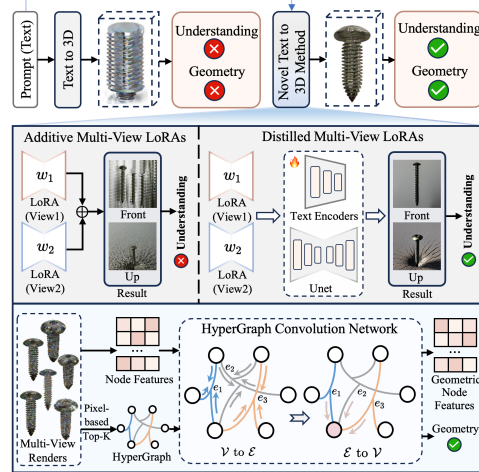


Figure 1. Overall Framework Architecture: Multi-Expert LoRA Ensemble Framework and Cross-View Hypergraph Enhancement

[44] and LucidDreamer [21], have demonstrated remarkable capabilities in generating imaginative 3D assets for creative applications. These methods typically leverage Score Distillation Sampling (SDS) [3, 22, 27] to distill knowledge from pretrained 2D diffusion models [12, 35–37] into 3D representations [28, 29, 43, 47], achieving impressive results for natural scene generation.

The field has witnessed rapid progress with diverse methodological innovations [13, 23, 25, 39, 40, 45, 52]. Era3D [20] introduced efficient row-wise attention for high-resolution multiview diffusion, while RichDreamer [33] enhanced detail richness through normal-depth diffusion models. Point-E [30] pioneered point cloud generation from complex prompts, and recent works like PI3D [24] and DreamPropeller [53] have further improved generation efficiency through pseudo-image diffusion and parallel sampling strategies. Additionally, consistency-focused approaches such as Consistent3D [48] have addressed deterministic sampling challenges,



Figure 2. Overview of custom-built multi-view industrial dataset and 3D generation results. The bottom-right image presents the corresponding 3D generation result produced by our method.

while subject-driven methods like DreamBooth3D [34] have enabled personalized 3D content creation.

However, despite significant progress in general-purpose text-to-3D generation, applying these techniques to industrial applications reveals critical limitations [16, 19, 46]. Industrial components like mechanical fasteners, electronic parts, and precision-machined surfaces demand both semantic accuracy and geometric precision that current approaches struggle to deliver. Existing methods face two fundamental challenges: (1) Domain Gap: models trained on natural scenes poorly understand industrial-specific semantics and geometric requirements; (2) Geometric Reasoning: traditional pairwise consistency constraints inadequately capture the complex structural dependencies essential for industrial precision, leading to artifacts in threading patterns, connector interfaces, and dimensional accuracy.

While Low-Rank Adaptation (LoRA) [4, 14, 50] offers a parameter-efficient approach for domain adaptation, conventional LoRA fusion strategies suffer from knowledge interference when combining multiple category-specific adaptations. Recent works have explored LoRA composition for image generation [18, 51] and domain bridging applications such as X-Dreamer [26], but the challenges of cross-category generalization in 3D domains remain largely unaddressed. Control-based approaches like DreamControl [15] have shown promise in enhancing text-to-3D generation with 3D self-priors, yet they still operate under domain-specific constraints that limit industrial applicability. Similarly, existing geometric consistency formulations [2, 42, 49], including the advanced Interval Score Matching approach [21], operate under pairwise assumptions [31, 38] that fail to capture the higher-order structural rela-

tionships [9, 10] crucial for industrial precision.

To address these challenges, we propose a systematic framework called ForgeDreamer for high-fidelity industrial text-to-3D generation that tackles the two fundamental limitations, as illustrated in Figure 1: (1) We address the semantic understanding challenge through a Multi-Expert LoRA Ensemble Framework that employs teacher-student knowledge distillation to consolidate multiple category-specific LoRA models into a unified representation, which achieves superior cross-category generalization for industrial domains. (2) Building on enhanced semantic understanding, we tackle the geometric precision challenge through Cross-View Hypergraph Geometric Enhancement. Drawing inspiration from hypergraph neural networks [6, 8], we formulate geometric consistency as a hypergraph learning problem that captures higher-order structural dependencies across multiple viewpoints simultaneously, moving beyond the limitations of pairwise consistency assumptions.

Moreover, existing industrial datasets such as MVTec 3D-AD [1] and Real-IAD[41] prove unsuitable for text-to-3D generation due to limited viewpoints and inconsistent imaging conditions (*see Appendix for experimental validation*). Therefore, we construct a controlled multi-view dataset for reliable text-to-3D industrial generation as shown in Figure 2.

Our framework operates on 3D Gaussian Splatting [17] for its superior efficiency in high-resolution rendering, essential for capturing intricate industrial details. Our main contributions are summarized as follows:

- We propose a novel teacher-student distillation framework that effectively consolidates multiple category-specific LoRA models into a unified representation, achieving superior cross-category generalization for industrial domains while avoiding knowledge interference.
- We introduce a Cross-View Hypergraph Enhanced Higher-Order Geometric Gradient Loss that captures structural dependencies spanning multiple viewpoints, addressing the fundamental limitations of pairwise geometric consistency assumptions.
- We conduct extensive experiments on a custom-built multi-view industrial dataset, demonstrating superior performance in both generation quality and semantic generalization compared to existing state-of-the-art methods.

2. Related Work

2.1. Text-to-3D Generation.

DreamFusion [32] pioneered text-to-3D generation through Score Distillation Sampling (SDS), which op-

timizes a 3D representation θ by minimizing:

$$\mathcal{L}_{\text{SDS}}(\theta) = \mathbb{E}_{t,\epsilon,c}[\omega(t)\|\epsilon(\mathbf{x}_t, t, y) - \epsilon\|_2^2] \quad (1)$$

where $\mathbf{x}_t = \sqrt{\bar{a}_t}\mathbf{x}_0 + \sqrt{1 - \bar{a}_t}\epsilon$ represents the noisy latent, and $\mathbf{x}_0 = g(\theta, c)$ is the rendered view. However, as analyzed in LucidDreamer [21], SDS suffers from over-smoothing due to inconsistent pseudo-ground-truths $\hat{\mathbf{x}}_0^t$. Recent works like ProlificDreamer [44] and LucidDreamer [21] have addressed this through Variational Score Distillation and Interval Score Matching respectively, but primarily focus on natural scenes rather than industrial domains.

2.2. Domain Adaptation Challenge.

Current text-to-3D models face a fundamental limitation when applied to industrial domains: semantic gap between natural scene training data and industrial object requirements.

Low-Rank Adaptation (LoRA) [14] enables efficient fine-tuning by decomposing weight updates as $\mathbf{W} = \mathbf{W}_0 + \mathbf{B}\mathbf{A}$, where $\mathbf{B} \in \mathbb{R}^{d \times r}$ and $\mathbf{A} \in \mathbb{R}^{r \times k}$ with rank $r \ll \min(d, k)$.

While individual LoRA adapters can capture category-specific knowledge, they suffer from knowledge isolation and lack cross-category generalization capabilities essential for diverse industrial applications.

Traditional LoRA fusion approaches employ simple additive combination, $\mathbf{W}_{\text{combined}} = \mathbf{W}_{\text{base}} + \sum_i \mathbf{W}_{\text{LoRA}}^{(i)}$. However, this naive fusion leads to knowledge interference where conflicting category-specific features degrade overall performance, as evidenced by the declining cosine similarity scores in Table 2 as the number of LoRAs increases.

2.3. Multi-View Geometric Consistency.

Existing text-to-3D methods rely on view-independent geometric constraints, treating consistency as pairwise optimization problems. LucidDreamer’s Interval Score Matching formulates consistency through interval-based score matching:

$$\mathcal{L}_{\text{ISM}}(\theta) = \mathbb{E}_{t,c}[\omega(t)\|\epsilon_\phi(\mathbf{x}_t, t, y) - \epsilon(\mathbf{x}_s, s, \Phi)\|_2^2] \quad (2)$$

where $s = t - \delta_T$. While effective, this approach still operates under pairwise assumptions and lacks the higher-order structural reasoning essential for complex industrial geometries with precise manufacturing requirements.

2.4. Industrial 3D Generation Challenges.

Current methods face fundamental limitations when applied to industrial domains: (1) semantic gap between natural scene training data and industrial object requirements, and (2) limited geometric reasoning

for precision-critical applications. Our work addresses these challenges through multi-expert knowledge consolidation and hypergraph-based geometric modeling that captures structural dependencies beyond pairwise relationships.

3. Methodology

Industrial text-to-3D generation faces two fundamental challenges that existing methods struggle to address effectively. First, direct application of pre-trained diffusion models to industrial domains suffers from poor semantic understanding and limited cross-category generalization, as these models are primarily trained on natural scene datasets. Second, existing models exhibit limited geometric reasoning capabilities, particularly in capturing higher-order structural dependencies essential for precise industrial geometries.

3.1. Overview

Figure 3 illustrates our systematic approach, named ForgeDreamer, to industrial text-to-3D generation, following a clear progression from semantic enhancement to geometric refinement to unified optimization: (1) Our Multi-Expert LoRA Ensemble Framework consolidates multiple category-specific LoRA models through teacher-student distillation, producing a unified representation that understands industrial component categories without knowledge interference. (2) Building on enhanced semantic understanding, our Cross-View Hypergraph Geometric Enhancement formulates consistency as a hypergraph learning problem, capturing higher-order structural dependencies across multiple viewpoints simultaneously. (3) We integrate both enhancements in an industrial-optimized pipeline where distilled LoRA weights provide semantic guidance while hypergraph modeling ensures geometric precision, together enabling high-fidelity industrial 3D generation. Overall, the key insight is that improving semantic understanding enables more effective geometric modeling, as the hypergraph operates on semantically meaningful features rather than poorly understood representations.

3.2. Multi-Expert LoRA Ensemble Framework

Industrial text-to-3D generation first requires robust semantic understanding of technical components. However, existing diffusion models trained on natural scenes lack domain-specific knowledge for industrial objects. While individual LoRA adapters can capture category-specific features, they suffer from knowledge isolation and interference when combined.

To address these limitations, we propose a teacher-student distillation framework that consolidates multiple

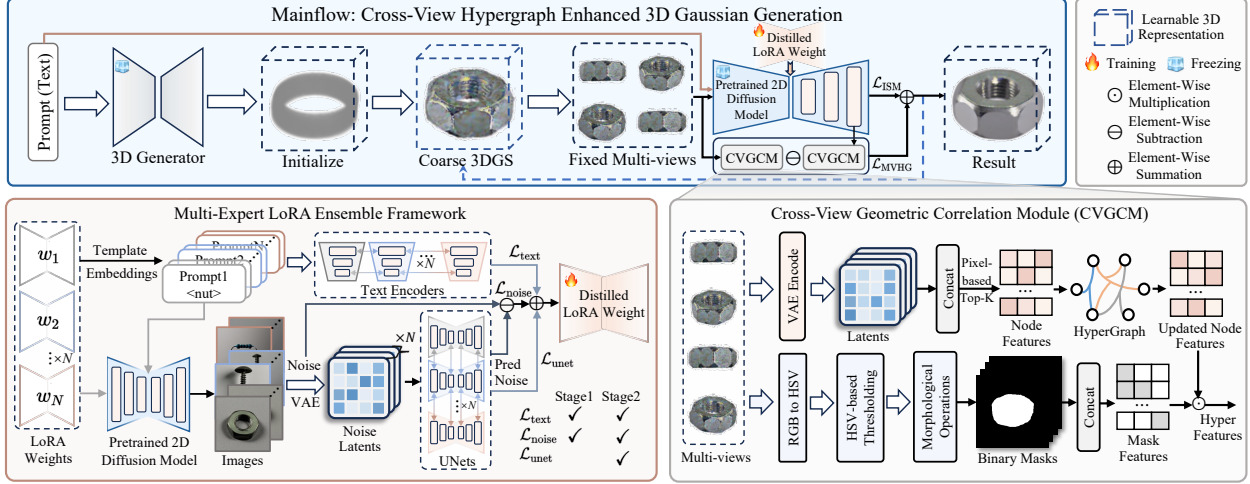


Figure 3. Architecture of our industrial Text-to-3D generation framework - ForgeDreamer. Top: Cross-view Hypergraph Enhanced 3D Gaussian Generation pipeline with Cross-View Geometric Correlation Module (CVGCM). Bottom: Multi-Expert LoRA Ensemble Framework for cross-category industrial knowledge integration.

category-specific LoRA experts into a unified representation, enabling cross-category generalization while preserving domain expertise.

3.2.1. Teacher-Student Architecture Construction.

Given a set of pre-trained LoRA weights $\{\mathcal{L}_i\}_{i=1}^N$ with corresponding trigger words $\{w_i\}_{i=1}^N$, we construct a teacher-student distillation architecture. Each teacher model T_i is formed by loading LoRA weights \mathcal{L}_i into the base Stable Diffusion model:

$$T_i = \text{SD}_{\text{base}} \oplus \mathcal{L}_i \quad (3)$$

where \oplus denotes the LoRA integration operation. Each teacher T_i specializes in generating high-quality samples for its corresponding trigger word w_i .

For each teacher T_i , we generate diverse 2D samples by incorporating multi-view prompts:

$$P_i^{\text{view}} = \text{A photo of a } \{\text{screw_front}\} / \{\text{screw_up}\}'$$

The generated images are encoded into latent space via VAE encoder: $z^{(i)} = \text{VAE}_{\text{enc}}(x^{(i)})$, forming individual datasets $D_i = (z^{(i)}, P_i^{\text{view}})$ for each teacher model. The complete distillation procedure is detailed in Algorithm 1.

In the first stage, we exclusively train the student model’s text encoder S_{text} while keeping the UNet frozen. This design prevents catastrophic forgetting and ensures stable feature learning. The second stage simultaneously optimizes both text encoder and UNet using an alternating training paradigm that switches between noise prediction and feature alignment at fixed intervals.

During training, we employ a round-robin strategy to ensure balanced knowledge transfer from all teachers.

Unlike additive fusion, our distillation approach learns to resolve conflicts by:

- The MSE-based alignment losses encourage the student to find a common feature space that accommodates all teacher expertise.
- The two-stage approach allows the model to first es-

Algorithm 1: Multi-LoRA Distillation

Input: LoRA weights $\{\mathcal{L}_i\}_{i=1}^N$, triggers $\{w_i\}_{i=1}^N$
Output: Distilled student model S

- 1 **for each** \mathcal{L}_i, w_i **do**
 - 2 Load \mathcal{L}_i into teacher T_i , sample with w_i
 - 3 \mathcal{D}_i : VAE-encoded latent–text pairs
 - 4 Initialize student model S
 - 5 **Stage 1: Train Text Encoder**
 - 6 **for each** $(T_i, (x_{\text{latent}}, w_i))$ from datasets $\{\mathcal{D}_i\}$ **do**
 - 7 $\mathcal{L}_{\text{text}} = \sum_l \alpha_l \cdot \text{MSE}(\text{Pool}(\mathbf{f}_T^l), \text{Pool}(\mathbf{f}_S^l))$;
 // \mathbf{f} : text encoder features
 - 8 $\mathcal{L}_{\text{noise}} = \text{MSE}(\hat{\epsilon}_S, \epsilon)$
 - 9 Update S_{text} with $\lambda_1^{\text{adp}} \mathcal{L}_{\text{text}} + \lambda_2^{\text{adp}} \mathcal{L}_{\text{noise}}$
 - 10 **Stage 2: Train Text Encoder & UNet**
 - 11 **for each** $(T_i, (x_{\text{latent}}, w_i))$ from datasets $\{\mathcal{D}_i\}$ **do**
 - 12 $\mathcal{L}_{\text{text}} = \sum_l \alpha_l \cdot \text{MSE}(\text{Pool}(\mathbf{f}_T^l), \text{Pool}(\mathbf{f}_S^l))$
 - 13 $\mathcal{L}_{\text{unet}} = \sum_m \beta_m \cdot \text{MSE}(\mathbf{u}_T^m, \mathbf{u}_S^m)$;
 // aligned UNet features
 - 14 $\mathcal{L}_{\text{noise}} = \text{MSE}(\hat{\epsilon}_S, \epsilon)$
 - 15 Update S with
 $\gamma_1^{\text{adp}} \mathcal{L}_{\text{text}} + \gamma_2^{\text{adp}} \mathcal{L}_{\text{unet}} + \gamma_3^{\text{adp}} \mathcal{L}_{\text{noise}}$
 - 16 **return** S
-

establish a stable semantic foundation before integrating complex geometric reasoning.

By incorporating view-specific training data, the distilled model learns to maintain semantic consistency across different perspectives, crucial for industrial 3D generation where viewpoint-dependent features are essential.

3.3. Cross-view Hypergraph Enhanced Higher-Order Geometric Gradient Loss

While our distilled LoRA provides enhanced semantic understanding, industrial 3D generation demands geometric precision that goes beyond semantic accuracy. Traditional pairwise consistency constraints fail to capture the higher-order structural dependencies essential for precision manufacturing.

Thus, we formulate geometric consistency as a hypergraph learning problem, capturing structural dependencies across multiple viewpoints simultaneously rather than treating them as independent pairwise constraints.

3.3.1. Hypergraph Geometric Modeling.

Unlike direct operations on point clouds [5], we first propose a cross-view hypergraph formulation that fundamentally shifts from pairwise to higher-order geometric reasoning. Given multi-view latent representations $\mathbf{Z} = \{\mathbf{z}^{(i)} \in \mathbb{R}^{H \times W \times C}\}_{i=1}^N$, we first construct a unified node feature representation by treating each pixel as an individual node.

For each view i , we reshape the latent representation $\mathbf{z}^{(i)} \in \mathbb{R}^{H \times W \times C}$ into a flattened format and concatenate across all views to form a comprehensive node feature matrix:

$$\mathbf{F} = \text{Concat}([\mathbf{z}_{\text{flat}}^{(1)}, \mathbf{z}_{\text{flat}}^{(2)}, \dots, \mathbf{z}_{\text{flat}}^{(N)}]) \in \mathbb{R}^{(N \cdot H \cdot W) \times C} \quad (4)$$

where $\mathbf{z}_{\text{flat}}^{(i)} \in \mathbb{R}^{(H \cdot W) \times C}$ represents the flattened latent features from view i . This results in a node feature matrix $\mathbf{F} \in \mathbb{R}^{(4 \cdot 64 \cdot 64) \times 4}$ for our experimental setup with 4 views and 4-dimensional latent channels.

Unlike conventional approaches that rely on spatial correspondence, we construct hypergraph $\mathcal{H} = (\mathcal{V}, \mathcal{E})$ through feature-based similarity relationships. For each node v_i represented by feature vector \mathbf{f}_i (the i -th row of \mathbf{F}), we establish hyperedges by computing feature similarities with all other nodes:

$$e_i = \{v_j : v_j \in \text{TopK}(\text{sim}(\mathbf{f}_i, \mathbf{f}_j), k)\} \quad (5)$$

where $\text{sim}(\cdot, \cdot)$ computes the cosine similarity between feature vectors, and $\text{TopK}(\cdot, k)$ selects the k most similar nodes to form a hyperedge. This feature-driven hyperedge construction enables the model to discover semantic and geometric correspondences across multiple

viewpoints that may not align spatially but share similar structural characteristics.

3.3.2. Cross-View Geometric Consistency Through Hypergraph Neural Networks.

We formulate geometric consistency as a hypergraph learning problem. Hypergraph Neural Networks (HGNN) is employed to aggregate cross-view geometric information through iterative message passing:

$$\mathbf{h}_v^{(l+1)} = \sigma(\mathbf{W}^{(l)} \sum_{e \in \mathcal{E}(v)} \frac{1}{|\mathcal{E}(v)|} \text{AGG}(\{\mathbf{h}_u^{(l)} : u \in e\})) \quad (6)$$

where $\mathbf{h}_v^{(l)}$ represents the feature vector of node v at layer l , $\mathcal{E}(v)$ denotes the set of hyperedges incident to node v , and uniform weighting $\frac{1}{|\mathcal{E}(v)|}$ balances aggregation across all connected hyperedges, and $\text{AGG}(\cdot)$ denotes an aggregation function that combines feature vectors from all nodes within each hyperedge into a unified representation [7].

Through this formulation, the hypergraph architecture naturally captures group-wise dependencies essential for industrial geometries, where structural precision depends on maintaining consistent relationships across multiple perspectives simultaneously, which represents a paradigm shift from local geometric optimization to global structural reasoning.

After hypergraph processing and mask-guided focus on object regions \mathcal{M} , our MVHG loss operates in the joint cross-view feature space:

$$\mathcal{L}_{\text{MVHG}} = \frac{1}{|\mathcal{M}|} \sum_{(h,w) \in \mathcal{M}} \left\| \mathbf{F}_z^{\text{masked}}[h, w, :] - \mathbf{F}_{\text{pred}}^{\text{masked}}[h, w, :] \right\|_2^2 \quad (7)$$

where $\mathbf{F}_z^{\text{masked}}$ and $\mathbf{F}_{\text{pred}}^{\text{masked}}$ represent the hypergraph-processed features from ground truth and predicted latents respectively, masked to focus on object regions. The step-by-step computation process is summarized in Algorithm 2.

3.4. ForgeDreamer: Unified Industrial Text-to-3D Pipeline

Having established semantic understanding through LoRA distillation and geometric modeling through hypergraph enhancement, we now integrate these components into a unified pipeline optimized for industrial applications.

Our industrial-oriented pipeline employs a unified optimization objective that simultaneously addresses semantic understanding and geometric precision:

$$\mathcal{L}_{\text{total}} = \lambda_{\text{ISM}} \mathcal{L}_{\text{ISM}} + \lambda_{\text{MVHG}} \mathcal{L}_{\text{MVHG}} \quad (8)$$

where \mathcal{L}_{ISM} ensures consistent pseudo-ground-truth generation through interval score matching, and $\mathcal{L}_{\text{MVHG}}$ enforces cross-view geometric consistency via our hypergraph formulation. This dual-objective design addresses the unique challenges of industrial 3D generation where both textual precision and geometric accuracy are critical.

Our framework utilizes 3D Gaussian Splatting for its superior efficiency in high-resolution rendering, essential for capturing intricate industrial details. The key insight is that our distilled LoRA weights improve the diffusion model’s understanding of industrial product categories. The CVGCM module operates continuously throughout training, extracting higher-order geometric relationships across multiple viewpoints. We employ fixed multi-view sampling optimized for industrial objects, providing standardized geometric supervision that maintains manufacturing precision and dimensional accuracy across different component categories. The combination of distilled industrial knowledge and hypergraph geometric modeling ensures that these structural details are both visually coherent and geometrically consistent across all viewpoints.

Algorithm 2: $\mathcal{L}_{\text{MVHG}}$ Computation

Input: Image batch \mathbf{X} , prompt c , training steps T , batch size B

Output: $\mathcal{L}_{\text{MVHG}}$

- 1 **for** $t = 1$ **to** T **do**
- 2 Encode: $\mathbf{Z} = \text{VAE}(\mathbf{X})$
- 3 Add noise: $\mathbf{Z}_{\text{noisy}} = \mathbf{Z} + \epsilon$, $\epsilon \sim \mathcal{N}(0, \sigma^2)$
- 4 Denoise: $\hat{\mathbf{X}}, \hat{\epsilon} = \text{SD}(\mathbf{Z}_{\text{noisy}}, c)$
- 5 Predict: $\mathbf{Z}_{\text{pred}} = \mathbf{Z}_{\text{noisy}} - \hat{\epsilon}$
- 6 Masks:
 $\mathbf{M}, \hat{\mathbf{M}} = \text{HSVMask}(\mathbf{X}), \text{HSVMask}(\hat{\mathbf{X}})$
- 7 Concat:
 $\mathbf{z} = \text{concat}(\mathbf{Z}), \mathbf{z}_{\text{pred}} = \text{concat}(\mathbf{Z}_{\text{pred}})$
- 8 Concat: $\mathbf{m} = \text{concat}(\mathbf{M}), \hat{\mathbf{m}} = \text{concat}(\hat{\mathbf{M}})$
- 9 Hypergraphs:
 $H_{\mathbf{z}}, H_{\text{pred}} = \text{TopK}(\mathbf{z}), \text{TopK}(\mathbf{z}_{\text{pred}})$
- 10 HGNN:
 $\mathbf{F}_{\mathbf{z}}, \mathbf{F}_{\text{pred}} = \text{HGNN}(H_{\mathbf{z}}), \text{HGNN}(H_{\text{pred}})$
- 11 Masked feats: $\mathbf{F}'_{\mathbf{z}}, \mathbf{F}'_{\text{pred}} = \mathbf{F}_{\mathbf{z}} \cdot \mathbf{m}, \mathbf{F}_{\text{pred}} \cdot \hat{\mathbf{m}}$
- 12 Loss: $\mathcal{L}_{\text{MVHG}} = \|\mathbf{F}'_{\mathbf{z}} - \mathbf{F}'_{\text{pred}}\|_2^2$
- 13 **return** $\mathcal{L}_{\text{MVHG}}$

In inference, our system operates through a coordinated multi-stage process that leverages both components synergistically. The pipeline begins with semantic-guided initialization, where text input is processed through our distilled LoRA-enhanced encoding

to produce an initial 3D Gaussian representation. Subsequently, the system enters an iterative multi-view consistency enforcement loop where each iteration renders multi-view images from the current 3D Gaussian Splatting representation, applies CVGCM processing to capture cross-view dependencies, and updates the 3D parameters based on both semantic and geometric losses.

4. Experiments

4.1. Dataset Construction and Specification

To obtain reliable supervision for LoRA distillation, we constructed a small, controlled multi-view dataset covering ten industrial categories: six mechanical components (screw, nut, bearing, gasket, nail, and hexagonal stud) and four electronic components (ceramic capacitor, resistor, red LED, and green LED). Each category contains 20 high-resolution images captured from front and top perspectives. Further dataset details are provided in the *Appendix*.

4.2. Text-to-3D Generation.

To evaluate the overall effectiveness of our generation pipeline, we begin by visualizing representative 3D assets synthesized from textual prompts. As shown in Figure 4, our proposed method produces semantically accurate 3D shapes with rich structural fidelity. Compared to prior methods primarily designed for natural scene generation, our framework exhibits superior performance in terms of topological coherence, edge sharpness, and texture consistency. For instance, prompts such as “a metallic screw with clear threads” or “a red LED” yield geometries that not only align with human expectations but also preserve shape-related priors and text-driven attributes. This improvement is largely attributed to the integration of distilled LoRA weights and the proposed higher-order hypergraph geometric loss, both of which contribute to capturing fine-grained structural details and enhancing semantic alignment in the generation process.

4.3. Qualitative Evaluation

We evaluate generation quality from three perspectives: (1) **image-based qualitative comparison**, (2) **quantitative evaluation** following the T3Bench [11] protocol, and (3) **LLM-based judgment** using a large language model as an external evaluator.

For qualitative comparison, we benchmark our method against several recent and representative Text-to-3D baselines, including ProlificDreamer [44] and RichDreamer [33] in their original forms, as well as DreamFusion [32] (with LoRA) and LucidDreamer [21] (with LoRA), which are adapted with distilled LoRA weights equivalent to those used in our approach. This



Figure 4. Qualitative Comparison with State-of-the-Art Methods. Visual results demonstrate the superior performance of our approach. See *Appendix* for remaining categories.

hybrid comparison setup allows us to assess both the baseline performance of existing models and the impact of integrating our LoRA distillation strategy under consistent conditions. A condensed quantitative comparison of processing time and average quality scores is provided in Table 1. All experiments are conducted on an NVIDIA RTX 4090 to ensure computational fairness. Representative qualitative results are shown in Figure 4, with additional comparisons on natural scenes provided in the *Appendix*.

Table 1. Condensed comparison of average scores (10 categories). [†]Total processing time; *Average T3Bench [11] quality score. Best and second-best scores are **bolded** and underlined, respectively. See *Appendix* for full results.

Method	Time [†]	Average*
ProlificDreamer [44] (w/o LoRA)	~10 hours	25.13
DreamFusion [32] (w/o LoRA)	6 hours	41.91
DreamFusion [32] (w/ LoRA)		44.83
RichDreamer [33] (w/o LoRA)	120 minutes	28.27
LucidDreamer [21] (w/o LoRA)	110 minutes	<u>47.10</u>
LucidDreamer [21] (w/ LoRA)		46.75
Ours	190 minutes	50.88

Across all ten categories, our method consistently produces exceptionally high-fidelity geometry, intricate detailed structures, photo-realistic materials, and out-

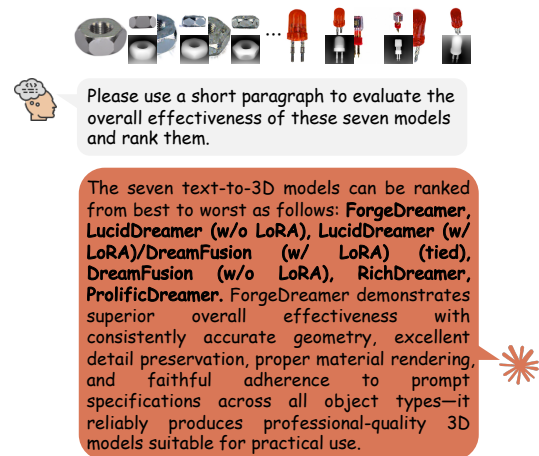


Figure 5. LLM-based qualitative ranking across ten object prompts, showing that our method achieves the highest overall fidelity and consistency. Full evaluation results are included in the *Appendix*.

standing prompt adherence, resulting in highly reliable and practical 3D asset generation suitable for downstream use. In notoriously demanding industrial-specific categories such as bolts, nuts, and connectors, our model notably and robustly preserves accurate topology and successfully avoids the typical artifacts such as disconnected geometry or unnatural surface oversmooth-

ing that plague other methods. The rigorous LLM-based comparative evaluation, which statistically confirms these advantages, is summarized in Figure 5.

4.4. Fine-tuning Strategy Analysis.

To evaluate different fine-tuning paradigms, we compare three variants of our framework. **No fine-tuning:** The base model without any domain-specific adaptation. **Single-LoRA adaptation:** Per-concept LoRA modules trained independently. **Multi-LoRA distillation:** Our proposed strategy merges multiple LoRAs into a unified model.

Figure 6 shows qualitative differences: the base model lacks fine structural detail, while Single-LoRA improves fidelity but struggles with generalization. Our Multi-LoRA distillation achieves the best trade-off, producing sharper geometry and consistent semantics across complex prompts. Table 2 complements this with quantitative evidence, showing that distillation maintains higher cosine similarity to original LoRAs compared to simple addition, especially as the number of fused LoRAs increases.

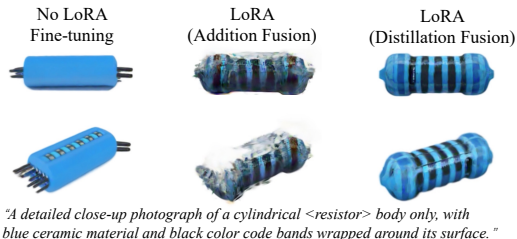


Figure 6. Multi-Expert LoRA Integration: Addition Fusion vs. Distillation Fusion

Table 2. Comparison of Average Concept Preservation Scores evaluated by CLIP-ViT-L/14. The full detailed table is presented in the *Appendix*.

Method	Two LoRAs	Four LoRAs	Six LoRAs
Addition	0.938	0.814	0.633
Distillation	0.965	0.949	0.952

4.5. Ablation Study

4.5.1. Effectiveness of MVHG Loss.

As shown in Figure 7, incorporating MVHG loss significantly improves the geometric fidelity and spatial consistency of the generated 3D shapes. Without it, models tend to produce artifacts such as inconsistent topology across views and distortions in fine structures. The MVHG loss introduces higher-order geometric constraints that capture inter-view correlations via a hypergraph representation, effectively regularizing complex surfaces and preserving overall shape in-

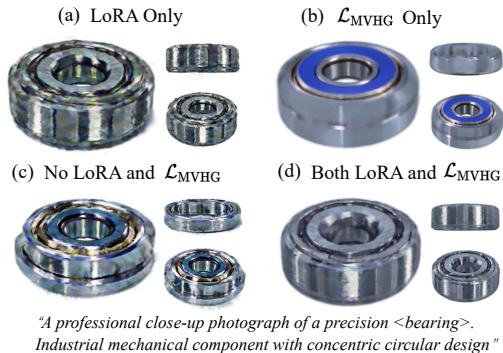


Figure 7. Component-wise Ablation Analysis: LoRA (Distillation Fusion) vs. MVHG Loss vs. Combined Approach

tegrity. These improvements underscore the importance of MVHG loss in enhancing structural coherence and reducing inter-view discrepancies in the synthesized results.

4.5.2. Influence of Distilled LoRA Fine-tuning.

We further assess the impact of our proposed Distilled LoRA fine-tuning approach on the overall performance of the text-to-3D generation pipeline. As illustrated in Figure 7, the absence of Distilled LoRA leads to a marked drop in visual plausibility and semantic alignment with input text prompts. Notably, models without our distillation framework often struggle to capture fine-grained attributes in underrepresented categories and exhibit unstable geometry when dealing with complex or multi-part semantics. In contrast, our Distilled LoRA effectively consolidates knowledge from multiple expert LoRAs, enhancing the model’s ability to encode domain-specific priors and adapt to subtle textual variations. This leads to more faithful and structurally coherent outputs.

5. Conclusion

In this paper, we present a novel framework, ForgeDreamer, for high-fidelity industrial text-to-3D generation that addresses two critical limitations of existing methods: domain adaptation challenges and geometric reasoning deficiencies. Our approach introduces two key innovations through a systematic progression: a Multi-Expert LoRA Geometric mechanism and a Cross-View Hypergraph Semantic Enhancement. The key contribution is to improve geometric precision through multi-expert LoRA, enabling more effective semantic modeling, while cross-view hypergraph understanding ensures precise geometric relationships across multiple views. Extensive experiments on our custom industrial dataset demonstrate superior performance compared to state-of-the-art methods, achieving enhanced semantic generalization and geometric fidelity for industrial components.

References

- [1] Paul Bergmann, Xin Jin, David Sattlegger, and Carsten Steger. The mvtec 3d-ad dataset for unsupervised 3d anomaly detection and localization. *arXiv preprint arXiv:2112.09045*, 2021. 2
- [2] Anpei Chen, Zexiang Xu, Fuqiang Zhao, Xiaoshuai Zhang, Fanbo Xiang, Jingyi Yu, and Hao Su. Mvs-nerf: Fast generalizable radiance field reconstruction from multi-view stereo. In *Proceedings of the IEEE/CVF international conference on computer vision*, pages 14124–14133, 2021. 2
- [3] Rui Chen, Yongwei Chen, Ningxin Jiao, and Kui Jia. Fantasia3d: Disentangling geometry and appearance for high-quality text-to-3d content creation. In *Proceedings of the IEEE/CVF international conference on computer vision*, pages 22246–22256, 2023. 1
- [4] Tim Dettmers, Artidoro Pagnoni, Ari Holtzman, and Luke Zettlemoyer. Qlora: Efficient finetuning of quantized llms, 2023. URL <https://arxiv.org/abs/2305.14314>, 2, 2023. 2
- [5] Donglin Di, Jiahui Yang, Chaofan Luo, Zhou Xue, Wei Chen, Xun Yang, and Yue Gao. Hyper-3dg: Text-to-3d gaussian generation via hypergraph. *International Journal of Computer Vision*, 133(5):2886–2909, 2025. 5
- [6] Yifan Feng, Haoxuan You, Zizhao Zhang, Rongrong Ji, and Yue Gao. Hypergraph neural networks. In *Proceedings of the AAAI conference on artificial intelligence*, pages 3558–3565, 2019. 2
- [7] Yifan Feng, Jiangang Huang, Shaoyi Du, Shihui Ying, Jun-Hai Yong, Yipeng Li, Guiguang Ding, Rongrong Ji, and Yue Gao. Hyper-yolo: When visual object detection meets hypergraph computation. *IEEE Transactions on Pattern Analysis and Machine Intelligence*, 2024. 5
- [8] Yue Gao, Yifan Feng, Shuyi Ji, and Rongrong Ji. Hgmn+: General hypergraph neural networks. *IEEE Transactions on Pattern Analysis and Machine Intelligence*, 45(3):3181–3199, 2022. 2
- [9] Kyle Genova, Forrester Cole, Avneesh Sud, Aaron Sarna, and Thomas Funkhouser. Local deep implicit functions for 3d shape. In *Proceedings of the IEEE/CVF conference on computer vision and pattern recognition*, pages 4857–4866, 2020. 2
- [10] Thibault Groueix, Matthew Fisher, Vladimir G Kim, Bryan C Russell, and Mathieu Aubry. A papier-mâché approach to learning 3d surface generation. In *Proceedings of the IEEE conference on computer vision and pattern recognition*, pages 216–224, 2018. 2
- [11] Yuze He, Yushi Bai, Matthieu Lin, Wang Zhao, Yubin Hu, Jenny Sheng, Ran Yi, Juanzi Li, and Yong-Jin Liu. T³ bench: Benchmarking current progress in text-to-3d generation. *arXiv preprint arXiv:2310.02977*, 2023. 6, 7
- [12] Jonathan Ho, Ajay Jain, and Pieter Abbeel. Denoising diffusion probabilistic models. *Advances in neural information processing systems*, 33:6840–6851, 2020. 1
- [13] Yicong Hong, Kai Zhang, Jiuxiang Gu, Sai Bi, Yang Zhou, Difan Liu, Feng Liu, Kalyan Sunkavalli, Trung Bui, and Hao Tan. Lrm: Large reconstruction model for single image to 3d. *arXiv preprint arXiv:2311.04400*, 2023. 1
- [14] Edward J Hu, Yelong Shen, Phillip Wallis, Zeyuan Allen-Zhu, Yuanzhi Li, Shean Wang, Lu Wang, Weizhu Chen, et al. Lora: Low-rank adaptation of large language models. *ICLR*, 1(2):3, 2022. 2, 3
- [15] Tianyu Huang, Yihan Zeng, Zhilu Zhang, Wan Xu, Hang Xu, Songcen Xu, Rynson WH Lau, and Wangmeng Zuo. Dreamcontrol: Control-based text-to-3d generation with 3d self-prior. In *Proceedings of the IEEE/CVF conference on computer vision and pattern recognition*, pages 5364–5373, 2024. 2
- [16] Benjamin Jones, Dalton Hildreth, Duowen Chen, Ilya Baran, Vladimir G Kim, and Adriana Schulz. Automate: A dataset and learning approach for automatic mating of cad assemblies. *ACM Transactions on Graphics (TOG)*, 40(6):1–18, 2021. 2
- [17] Bernhard Kerbl, Georgios Kopanas, Thomas Leimkühler, and George Drettakis. 3d gaussian splatting for real-time radiance field rendering. *ACM Trans. Graph.*, 42(4):139–1, 2023. 2
- [18] Nupur Kumari, Bingliang Zhang, Richard Zhang, Eli Shechtman, and Jun-Yan Zhu. Multi-concept customization of text-to-image diffusion. In *Proceedings of the IEEE/CVF conference on computer vision and pattern recognition*, pages 1931–1941, 2023. 2
- [19] Joseph G Lambourne, Karl DD Willis, Pradeep Kumar Jayaraman, Aditya Sanghi, Peter Meltzer, and Hooman Shayani. Brepnet: A topological message passing system for solid models. In *Proceedings of the IEEE/CVF conference on computer vision and pattern recognition*, pages 12773–12782, 2021. 2
- [20] Peng Li, Yuan Liu, Xiaoxiao Long, Feihu Zhang, Cheng Lin, Mengfei Li, Xingqun Qi, Shanghang Zhang, Wei Xue, Wenhan Luo, et al. Era3d: High-resolution multiview diffusion using efficient row-wise attention. *Advances in Neural Information Processing Systems*, 37:55975–56000, 2024. 1
- [21] Yixun Liang, Xin Yang, Jiantao Lin, Haodong Li, Xiaogang Xu, and Yingcong Chen. Luciddreamer: Towards high-fidelity text-to-3d generation via interval score matching. In *Proceedings of the IEEE/CVF conference on computer vision and pattern recognition*, pages 6517–6526, 2024. 1, 2, 3, 6, 7
- [22] Chen-Hsuan Lin, Jun Gao, Luming Tang, Towaki Takikawa, Xiaohui Zeng, Xun Huang, Karsten Kreis, Sanja Fidler, Ming-Yu Liu, and Tsung-Yi Lin. Magic3d: High-resolution text-to-3d content creation. In *Proceedings of the IEEE/CVF conference on computer vision and pattern recognition*, pages 300–309, 2023. 1
- [23] Ruoshi Liu, Rundi Wu, Basile Van Hoorick, Pavel Tokmakov, Sergey Zakharov, and Carl Vondrick. Zero-1-to-3: Zero-shot one image to 3d object. In *Proceedings of the IEEE/CVF international conference on computer vision*, pages 9298–9309, 2023. 1
- [24] Ying-Tian Liu, Yuan-Chen Guo, Guan Luo, Heyi Sun, Wei Yin, and Song-Hai Zhang. Pi3d: Efficient text-to-3d generation with pseudo-image diffusion. In *Proceedings*

- of the *IEEE/CVF Conference on Computer Vision and Pattern Recognition*, pages 19915–19924, 2024. 1
- [25] Shitong Luo and Wei Hu. Diffusion probabilistic models for 3d point cloud generation. In *Proceedings of the IEEE/CVF conference on computer vision and pattern recognition*, pages 2837–2845, 2021. 1
- [26] Yiwei Ma, Yijun Fan, Jiayi Ji, Haowei Wang, Haibing Yin, Xiaoshuai Sun, and Rongrong Ji. Creating high-quality 3d content by bridging the gap between text-to-2d and text-to-3d generation. *ACM Transactions on Multimedia Computing, Communications and Applications*, 2024. 2
- [27] Gal Metzger, Elad Richardson, Or Patashnik, Raja Giryes, and Daniel Cohen-Or. Latent-nerf for shape-guided generation of 3d shapes and textures. In *Proceedings of the IEEE/CVF conference on computer vision and pattern recognition*, pages 12663–12673, 2023. 1
- [28] Ben Mildenhall, Pratul P Srinivasan, Matthew Tancik, Jonathan T Barron, Ravi Ramamoorthi, and Ren Ng. Nerf: Representing scenes as neural radiance fields for view synthesis. *Communications of the ACM*, 65(1):99–106, 2021. 1
- [29] Thomas Müller, Alex Evans, Christoph Schied, and Alexander Keller. Instant neural graphics primitives with a multiresolution hash encoding. *ACM transactions on graphics (TOG)*, 41(4):1–15, 2022. 1
- [30] Alex Nichol, Heewoo Jun, Prafulla Dhariwal, Pamela Mishkin, and Mark Chen. Point-e: A system for generating 3d point clouds from complex prompts. *arXiv preprint arXiv:2212.08751*, 2022. 1
- [31] Michael Niemeyer and Andreas Geiger. Giraffe: Representing scenes as compositional generative neural feature fields. In *Proceedings of the IEEE/CVF conference on computer vision and pattern recognition*, pages 11453–11464, 2021. 2
- [32] Ben Poole, Ajay Jain, Jonathan T Barron, and Ben Mildenhall. Dreamfusion: Text-to-3d using 2d diffusion. *arXiv preprint arXiv:2209.14988*, 2022. 1, 2, 6, 7
- [33] Lingteng Qiu, Guanying Chen, Xiaodong Gu, Qi Zuo, Mutian Xu, Yushuang Wu, Weihao Yuan, Zilong Dong, Liefeng Bo, and Xiaoguang Han. Richdreamer: A generalizable normal-depth diffusion model for detail richness in text-to-3d. In *Proceedings of the IEEE/CVF conference on computer vision and pattern recognition*, pages 9914–9925, 2024. 1, 6, 7
- [34] Amit Raj, Srinivas Kaza, Ben Poole, Michael Niemeyer, Nataniel Ruiz, Ben Mildenhall, Shiran Zada, Kfir Aberman, Michael Rubinstein, Jonathan Barron, et al. Dreambooth3d: Subject-driven text-to-3d generation. In *Proceedings of the IEEE/CVF international conference on computer vision*, pages 2349–2359, 2023. 2
- [35] Aditya Ramesh, Prafulla Dhariwal, Alex Nichol, Casey Chu, and Mark Chen. Hierarchical text-conditional image generation with clip latents. *arXiv preprint arXiv:2204.06125*, 1(2):3, 2022. 1
- [36] Robin Rombach, Andreas Blattmann, Dominik Lorenz, Patrick Esser, and Björn Ommer. High-resolution image synthesis with latent diffusion models. In *Proceedings of the IEEE/CVF conference on computer vision and pattern recognition*, pages 10684–10695, 2022.
- [37] Chitwan Saharia, William Chan, Saurabh Saxena, Lala Li, Jay Whang, Emily L Denton, Kamyar Ghasemipour, Raphael Gontijo Lopes, Burcu Karagol Ayan, Tim Salimans, et al. Photorealistic text-to-image diffusion models with deep language understanding. *Advances in neural information processing systems*, 35:36479–36494, 2022. 1
- [38] Katja Schwarz, Yiyi Liao, Michael Niemeyer, and Andreas Geiger. Graf: Generative radiance fields for 3d-aware image synthesis. *Advances in neural information processing systems*, 33:20154–20166, 2020. 2
- [39] Yichun Shi, Peng Wang, Jianglong Ye, Mai Long, Kejie Li, and Xiao Yang. Mvdream: Multi-view diffusion for 3d generation. *arXiv preprint arXiv:2308.16512*, 2023. 1
- [40] Jiaming Song, Chenlin Meng, and Stefano Ermon. Denoising diffusion implicit models. *arXiv preprint arXiv:2010.02502*, 2020. 1
- [41] Chengjie Wang, Wenbing Zhu, Bin-Bin Gao, Zhenye Gan, Jiangning Zhang, Zhihao Gu, Shuguang Qian, Mingang Chen, and Lizhuang Ma. Real-iad: A real-world multi-view dataset for benchmarking versatile industrial anomaly detection. In *Proceedings of the IEEE/CVF Conference on Computer Vision and Pattern Recognition*, pages 22883–22892, 2024. 2
- [42] Qianqian Wang, Zhicheng Wang, Kyle Genova, Pratul P Srinivasan, Howard Zhou, Jonathan T Barron, Ricardo Martin-Brualla, Noah Snavely, and Thomas Funkhouser. Ibrnet: Learning multi-view image-based rendering. In *Proceedings of the IEEE/CVF conference on computer vision and pattern recognition*, pages 4690–4699, 2021. 2
- [43] Zirui Wang, Shangzhe Wu, Weidi Xie, Min Chen, and Victor Adrian Prisacariu. Nerf-: Neural radiance fields without known camera parameters. 2021. 1
- [44] Zhengyi Wang, Cheng Lu, Yikai Wang, Fan Bao, Chongxuan Li, Hang Su, and Jun Zhu. Prolificdreamer: High-fidelity and diverse text-to-3d generation with variational score distillation. *Advances in neural information processing systems*, 36:8406–8441, 2023. 1, 3, 6, 7
- [45] Daniel Watson, Jonathan Ho, Mohammad Norouzi, and William Chan. Learning to efficiently sample from diffusion probabilistic models. *arXiv preprint arXiv:2106.03802*, 2021. 1
- [46] Karl DD Willis, Pradeep Kumar Jayaraman, Hang Chu, Yunsheng Tian, Yifei Li, Daniele Grandi, Aditya Sanghi, Linh Tran, Joseph G Lambourne, Armando Solar-Lezama, et al. Joinable: Learning bottom-up assembly of parametric cad joints. In *Proceedings of the IEEE/CVF conference on computer vision and pattern recognition*, pages 15849–15860, 2022. 2
- [47] Tong Wu, Yu-Jie Yuan, Ling-Xiao Zhang, Jie Yang, Yan-Pei Cao, Ling-Qi Yan, and Lin Gao. Recent advances in 3d gaussian splatting. *Computational Visual Media*, 10(4):613–642, 2024. 1
- [48] Zike Wu, Pan Zhou, Xuanyu Yi, Xiaoding Yuan, and Hanwang Zhang. Consistent3d: Towards consistent

- high-fidelity text-to-3d generation with deterministic sampling prior. In *Proceedings of the IEEE/CVF Conference on Computer Vision and Pattern Recognition*, pages 9892–9902, 2024. [1](#)
- [49] Alex Yu, Vickie Ye, Matthew Tancik, and Angjoo Kanazawa. pixelnerf: Neural radiance fields from one or few images. In *Proceedings of the IEEE/CVF conference on computer vision and pattern recognition*, pages 4578–4587, 2021. [2](#)
- [50] Qingru Zhang, Minshuo Chen, Alexander Bukharin, Nikos Karampatziakis, Pengcheng He, Yu Cheng, Weizhu Chen, and Tuo Zhao. Adalora: Adaptive budget allocation for parameter-efficient fine-tuning. *arXiv preprint arXiv:2303.10512*, 2023. [2](#)
- [51] Ming Zhong, Yelong Shen, Shuohang Wang, Yadong Lu, Yizhu Jiao, Siru Ouyang, Donghan Yu, Jiawei Han, and Weizhu Chen. Multi-lora composition for image generation. *arXiv preprint arXiv:2402.16843*, 2024. [2](#)
- [52] Linqi Zhou, Yilun Du, and Jiajun Wu. 3d shape generation and completion through point-voxel diffusion. In *Proceedings of the IEEE/CVF international conference on computer vision*, pages 5826–5835, 2021. [1](#)
- [53] Linqi Zhou, Andy Shih, Chenlin Meng, and Stefano Ermon. Dreampropeller: Supercharge text-to-3d generation with parallel sampling. In *Proceedings of the IEEE/CVF Conference on Computer Vision and Pattern Recognition*, pages 4610–4619, 2024. [1](#)

ForgeDreamer: Industrial Text-to-3D Generation with Multi-Expert LoRA and Cross-View Hypergraph

Supplementary Material

6. Appendix

6.1. Code and Dataset Examples

We provide example implementations of the key components of our method, ForgeDreamer—including the LoRA distillation pipeline and the cross-view hypergraph enhancement module—in the supplementary materials to facilitate reproducibility. In addition, sample data from our multi-view industrial dataset are also included in the supplement to illustrate the data format and preprocessing workflow.

6.2. Limitations of Existing Public 3D Datasets

Although widely used in industrial anomaly detection and 3D perception, existing public datasets such as MVTec 3D-AD and Real-IAD are not well suited for our LoRA distillation framework. MVTec 3D-AD provides RGB images paired with depth or point cloud data; however, these point clouds are often incomplete. When generating a front-view image, the lower portion of the geometry is frequently missing, making it impossible to obtain a consistent and fully visible front-view observation required for LoRA training.

Real-IAD suffers from a different limitation: the dataset supplies only two viewpoints for each object—an oblique 45° view and a strictly top-down view. Since no true front-view images are available, the dataset cannot support the dual-perspective (front and up) supervision that our method relies on to ensure stable and geometry-consistent LoRA adaptation.

To validate these limitations empirically, we conducted experiments using both datasets. As shown in Figure 9a and Figure 9b, models trained on MVTec 3D-AD and Real-IAD exhibit degraded 3D generation quality, including incomplete geometry reconstruction, unstable texture synthesis, and inconsistent cross-view appearance. These results further demonstrate that the characteristics of existing datasets prevent them from providing the clean, multi-view supervision required by our framework, thereby motivating the construction of our own dataset.

6.3. Dataset Construction and Specification

To train and evaluate our LoRA distillation framework, we constructed a multi-view dataset comprising ten object categories: six mechanical components (screw, nut, bearing, gasket, nail, hexagonal stud) and four electronic components (ceramic capacitor, resistor, red LED,

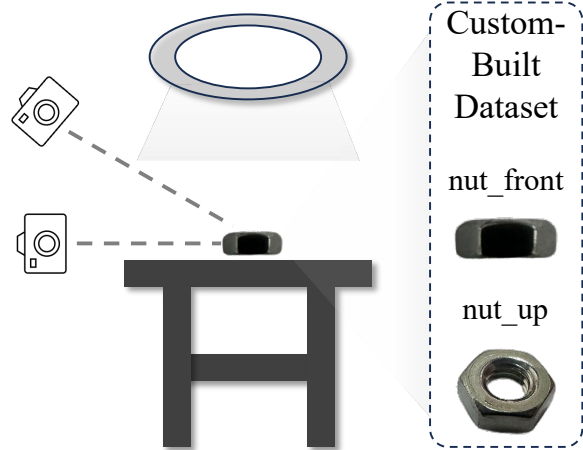
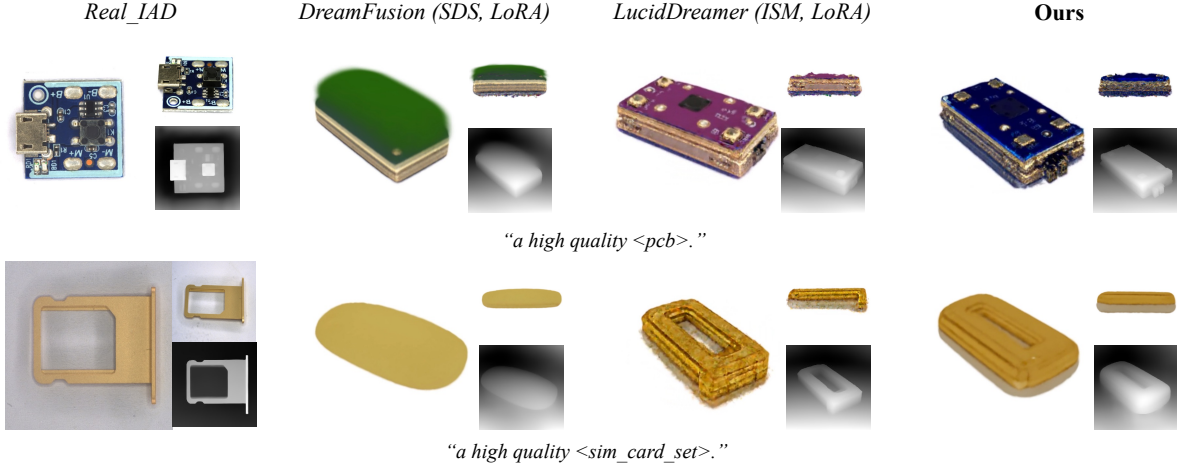


Figure 8. Our data capture apparatus (left) and collected dataset samples (right). The setup utilizes controlled lighting and fixed mounts to acquire consistent front and top-down view images for each industrial component.

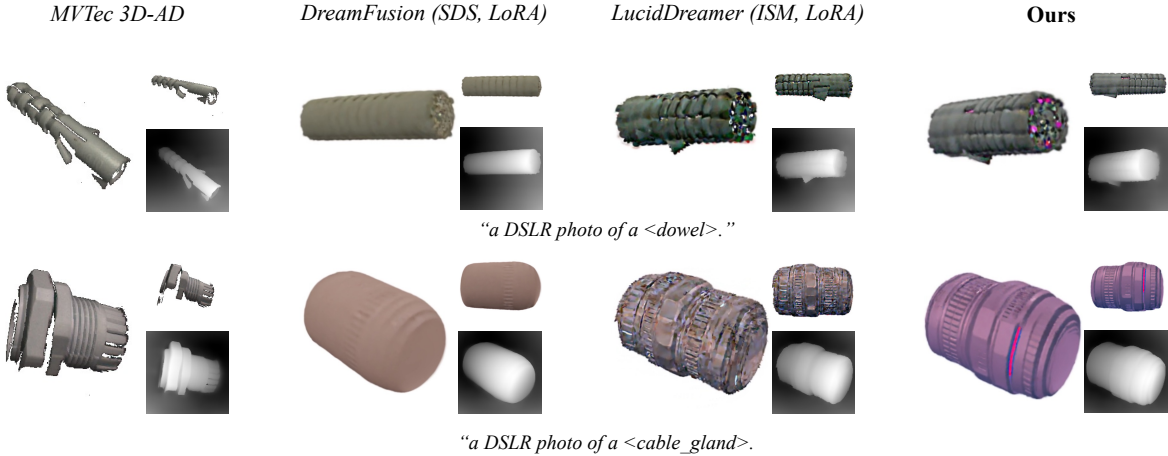
green LED). The dataset contains more than 200 high-resolution images (512×512 pixels), with 20 images per category evenly captured from front and up view perspectives. The data were collected using a standardized imaging setup equipped with a uniform ring-light illumination system, as illustrated schematically in Figure 8.

For each object category, we captured 10 front view images with objects positioned to show their primary functional surface, and 10 up view images photographed from directly above to reveal structural details. All images were acquired under controlled studio lighting with diffused illumination against a neutral white background, using fixed camera settings to ensure consistent quality and exposure. The standardized acquisition protocol enables comprehensive feature learning by providing dual perspectives that capture both surface textures and geometric characteristics essential for robust LoRA training.

The dataset underwent rigorous quality control including sharpness verification, exposure consistency checks, and annotation accuracy validation. This balanced multi-view configuration allows LoRAs to recognize objects from multiple perspectives while capturing fine-grained differences between similar categories. The equal distribution across categories and viewpoints prevents bias during LoRA adaptation and ensures stable training for the distillation process.



(a) Results on the Real-IAD dataset. Our method successfully identifies and localizes industrial defects.



(b) Comparison on the MVTec 3D-AD dataset. Our approach provides superior defect coverage compared to prior methods.

Figure 9. Qualitative results on two public industrial datasets. (a) Real-IAD: our method accurately detects and localizes defects. (b) MVTec 3D-AD: our framework achieves improved defect completeness and surface consistency.

6.4. Implementation Details

6.4.1. Distillation Phase Configuration.

The distillation process is structured as a two-stage training pipeline, designed to systematically transfer knowledge from the teacher experts to the unified student model. Both Stage 1 and Stage 2 follow identical training configurations. Each stage is trained for 5,000 iterations to ensure sufficient convergence of the student’s features while maintaining computational efficiency. We employ Low-Rank Adaptation (LoRA) with a rank parameter set to 16. This rank provides an optimal balance between parameter efficiency and model expressiveness, allowing the adapter to capture nuanced, domain-specific features without introducing excessive parameters. This LoRA configuration allows for effective fine-tuning while reducing the number of trainable parameters compared to full fine-tuning approaches.

6.4.2. ForgeDreamer Training Protocol.

The ForgeDreamer training process follows a schedule spanning 5,000 iterations. The training begins with a warm-up phase covering the initial 1,500 iterations, during which the learning rate increases to its target value. This warm-up strategy helps stabilize the early stages of training and prevents potential optimization instabilities from aggressive initial learning rates. Following this stabilization period, the remaining 3,500 iterations proceed with the training protocol.

During ForgeDreamer training, we maintain a batch size of 4 throughout the entire training process. This batch size was selected to achieve maximum training efficiency by utilizing the available VRAM on the NVIDIA RTX 4090 24G GPU, while also ensuring stable gradient updates and maintaining reproducible results across different experimental runs.

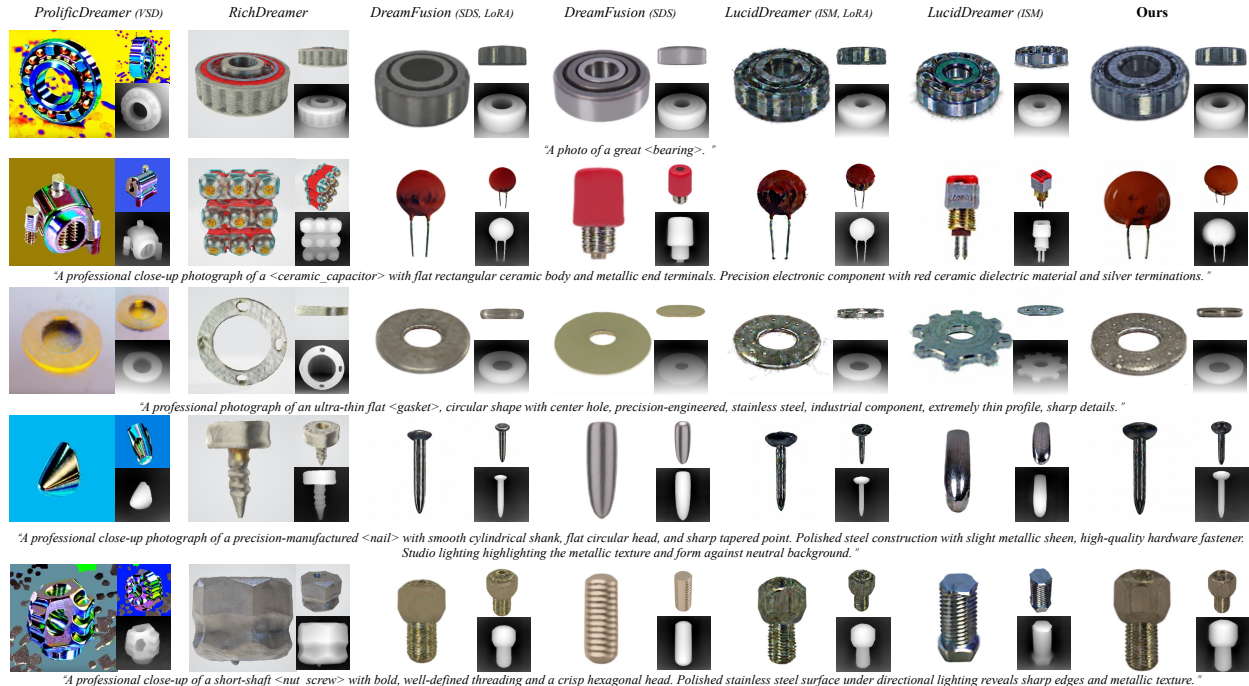


Figure 10. Qualitative Comparison with State-of-the-Art Methods. Visual results demonstrate the superior performance of our approach (remaining categories).

6.4.3. Hardware and Computational Environment.

All experimental procedures, including both the LoRA distillation phases and the complete ForgeDreamer training pipeline, are conducted on a single NVIDIA RTX 4090 24G GPU. This hardware configuration provides sufficient computational resources for the training requirements while maintaining accessibility for research purposes. The use of a single GPU setup ensures consistent experimental conditions and eliminates potential variations that might arise from distributed training configurations.

6.5. Additional Industrial Scene Results

We present further analysis under different industrial settings to thoroughly evaluate our method’s capabilities. This includes examining the performance when processing varying numbers of industrial objects, simulating real-world scenarios that range from single-object synthesis to more complex, populated scenes. To provide a more intuitive understanding of the generation quality differences, we visualize the detailed comparative results across these different experimental configurations.

As shown in Figure 10, which complements the visual results in the main paper, we include extended comparisons with additional baseline methods. This figure focuses on the remaining five industrial categories: **bearing, ceramic capacitor, gasket, nail, and hexagonal stud.**

These visual results clearly demonstrate the robustness and generality of our approach in industrial object generation. Across these categories, our method consistently produces higher-fidelity geometry, more accurate structural details (such as the threading on studs or contacts on capacitors), and avoids common failure modes like surface oversmoothing or disconnected parts that are visible in baseline results. The comprehensive analysis reveals consistent performance improvements across these different experimental configurations within the industrial domain.

6.6. Detailed LoRA Fusion Analysis

Detailed analysis of the LoRA fusion mechanisms reveals significant insights into the behavior of different fusion strategies across varying configurations. Through systematic evaluation of 2, 4, and 6 LoRA configurations, we investigate both quantitative performance metrics and underlying representational changes.

The visualizations in Figure 11, Figure 12, and Figure 13 present these analyses. The cosine similarity analysis (subplot a) provides a direct measurement of how well fused LoRAs preserve individual component characteristics, while PCA decomposition (subplot b) offers geometric insights into the structural relationships within the learned representation space.

To further quantify these findings, Table 3 provides a detailed comparison of concept preservation scores for

Table 3. Concept Preservation Scores by Fusion Method and LoRA Configuration

Method (CLIP-ViT-L/14)	Two LoRAs	Four LoRAs	Six LoRAs
<i>Individual Concepts</i>			
Emb1 (Addition)	0.899	0.793	0.658
Emb1 (Distillation)	0.927	0.934	0.904
Emb2 (Addition)	0.886	0.779	0.653
Emb2 (Distillation)	0.915	0.963	0.963
Emb3 (Addition)	—	0.855	0.708
Emb3 (Distillation)	—	0.972	0.968
Emb4 (Addition)	—	0.827	0.691
Emb4 (Distillation)	—	0.927	0.936
Emb5 (Addition)	—	—	0.630
Emb5 (Distillation)	—	—	0.969
Emb6 (Addition)	—	—	0.458
Emb6 (Distillation)	—	—	0.970
<i>Overall Performance</i>			
Average (Addition)	0.938	0.814	0.633
Average (Distillation)	0.965	0.949	0.952

our distillation method versus simple additive fusion. The data shows that our distillation method consistently and significantly outperforms additive fusion across all configurations (e.g., 0.952 vs. 0.633 average for six LoRAs), demonstrating its effectiveness in preventing catastrophic interference.

6.7. LLM-Based Qualitative Evaluation

To provide an objective and detailed qualitative assessment, we employed a Large Language Model (LLM) to evaluate and compare our method against the baselines. This qualitative feedback was then distilled into a quantitative ranking by tallying the LLM’s preferences across all comparisons, as summarized in Table 4. Table 4 details these results, where a lower rank indicates better user preference. Our method achieved the best possible rank (1.0) in 6 out of 10 categories for an average rank of 1.6, significantly outperforming all baselines and confirming its superior perceptual quality. The following Figures 15 to 18 present the complete, verbatim responses from the LLM evaluator, which form the basis of this analysis. This evaluation provides a comprehensive and unbiased analysis of the geometry, texture, and prompt adherence of the generated results across all ten industrial categories and additional prompts.

6.8. Natural Scene Generation Evaluation

To evaluate the generalizability of our approach beyond its primary industrial applications, we conducted a com-

parative analysis on common natural scene generation tasks. While ForgeDreamer is specifically designed and optimized for industrial object synthesis, we demonstrate that our unified LoRA fusion strategy still maintains highly competitive performance in these distinct natural scene contexts.

Figure 14 presents qualitative comparisons between our method and baseline approaches on “bagel” and “hamburger” objects. The results indicate that our fusion mechanism successfully preserves the critical semantic coherence and high visual quality necessary for natural image generation. Crucially, the specialized industrial-focused training does not unduly compromise the model’s ability to handle general-purpose generation tasks. This cross-domain evaluation validates that ForgeDreamer achieves its domain-specific optimization without sacrificing broader applicability, making it suitable for mixed industrial-natural generation scenarios that are commonly encountered in practical applications.

6.9. Per-Category T3Bench Scores

Table 5 presents the full breakdown of T3Bench quality scores across all ten industrial categories. This detailed data substantiates the findings from the main paper. It shows that our method not only achieves the highest average score (50.88) by a significant margin over the next-best competitor (47.10), but also secures a top-two result (best or second-best) in 7 out of the 10 categories.

Specifically, our method achieves the **number one** rank in four distinct categories: **G. LED**, **Screw**, **Bearing**, and **Gasket**. It also secures the **second-best** rank in three others: **R. LED**, **Hex Stud**, and **Nail**.

This demonstrates a high degree of robustness. It is particularly noteworthy that while some baselines (e.g., LucidDreamer w/o LoRA) achieve exceptionally high scores in a few specific categories where our method does not lead (such as **Nut** and **Capacitor**), they exhibit significant performance drops in others. In contrast, our method avoids catastrophic failures and maintains a high-quality baseline across the entire spectrum. This balance between high peak performance (achieving 1st place in 40% of categories) and strong consistency (placing in the top-two 70% of the time) is what drives the superior overall average score, confirming its robust generation quality for diverse industrial components. However, we believe this automated metric, while useful, does not fully reflect all perceptual nuances of generation quality and should be considered a strong reference rather than a complete assessment.

6.10. Cross-Configuration Analysis.

Comparing across all configurations (Figures 11, 12, and 13), we observe several consistent patterns that demonstrate the robustness of our approach:

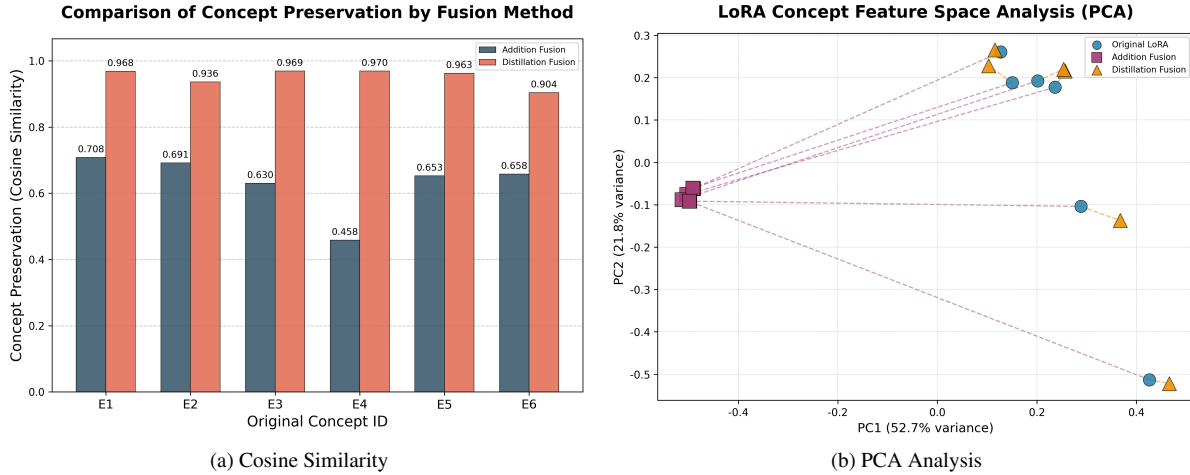


Figure 11. Analysis of Six LoRAs Configuration: (a) Cosine similarity comparison between addition fusion and ablation fusion methods. (b) PCA visualization showing the representational space distribution and relative distances to the original LoRA.

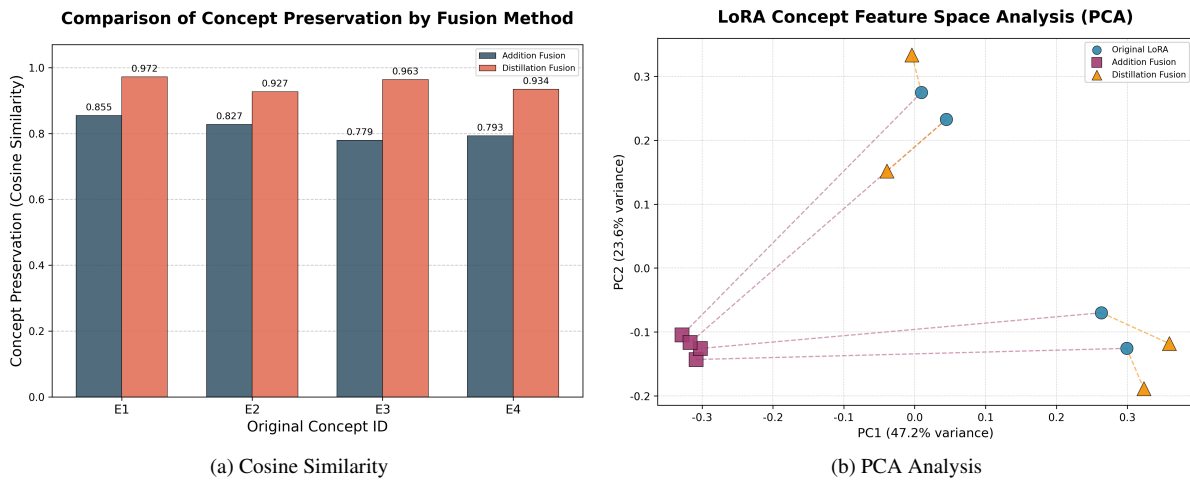


Figure 12. Analysis of Four LoRAs Configuration: (a) Cosine similarity metrics demonstrating the effectiveness of addition fusion over ablation fusion. (b) PCA decomposition revealing the structural relationships between fused LoRAs and the original representation.

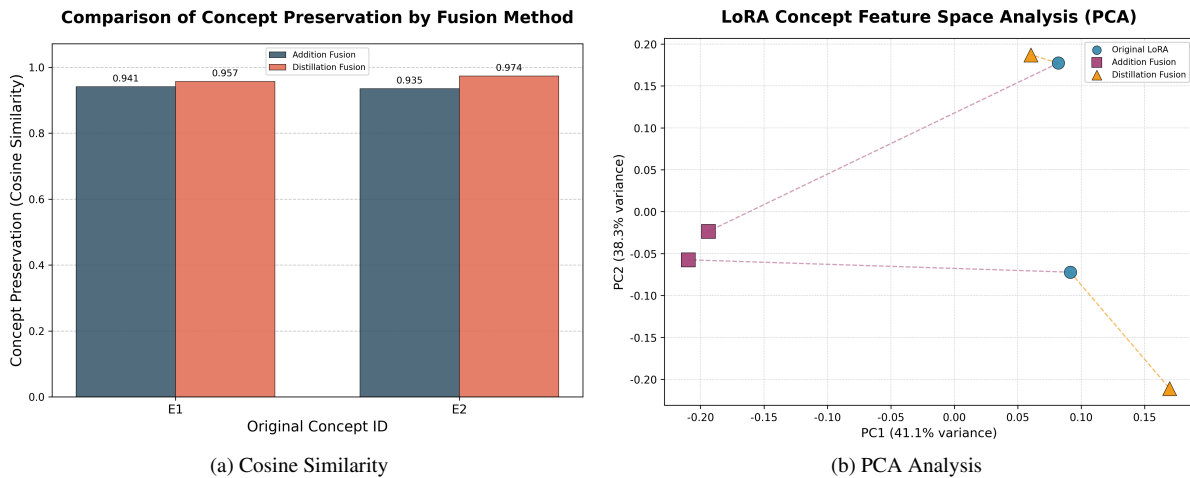


Figure 13. Analysis of Two LoRAs Configuration: (a) Cosine similarity comparison showing the fundamental differences between fusion approaches. (b) PCA analysis illustrating the simplest case of LoRA fusion and its impact on representational geometry.

Table 4. Quantitative user study ranking across ten object categories. Lower ranks are better. Best (rank 1) and second-best (rank 2) results in each column are highlighted in **bold** and underlined, respectively.

Method	G. LED	Nut	R. LED	Resistor	Screw	Bearing	Capacitor	Hex Stud	Nail	Gasket	Average
ProlificDreamer [44] (w/o LoRA)	7	7	7	7	7	7	7	7	7	6	6.9
RichDreamer [33] (w/o LoRA)	6	6	6	6	6	4	6	6	4	3	5.3
DreamFusion [32] (w/ LoRA)	3	5	2	2	2	2	4	2	1	1	2.4
DreamFusion [32] (w/o LoRA)	5	4	5	5	5	1	1	5	5	4	4.0
LucidDreamer [21] (w/LoRA)	<u>2</u>	3	3	3	4	6	5	4	3	5	3.8
LucidDreamer [21] (w/o LoRA)	4	<u>2</u>	4	4	3	5	<u>2</u>	3	6	7	4.0
Ours	1	1	1	1	1	3	3	1	<u>2</u>	<u>2</u>	1.6

Table 5. Quantitative comparison across ten object categories on T3Bench quality scores. Best and second-best results in each column are highlighted in **bold** and underlined, respectively.

Method	G. LED	Nut	R. LED	Resistor	Screw	Bearing	Capacitor	Hex Stud	Nail	Gasket	Average
ProlificDreamer [44] (w/o LoRA)	27.19	22.34	24.49	26.60	34.85	31.64	20.48	7.85	26.39	29.45	25.13
RichDreamer [33] (w/o LoRA)	17.21	42.26	15.58	<u>42.31</u>	38.33	21.24	17.83	24.38	39.90	23.70	28.27
DreamFusion [32] (w/o LoRA)	32.62	<u>69.72</u>	29.92	28.49	46.59	28.38	<u>35.45</u>	36.66	52.27	<u>59.02</u>	41.91
DreamFusion [32] (w/ LoRA)	48.27	63.31	31.98	38.40	56.29	22.76	21.12	50.61	62.27	53.27	44.83
LucidDreamer [21] (w/o LoRA)	44.46	71.37	31.24	53.23	53.97	<u>36.86</u>	45.51	58.93	39.66	35.72	<u>47.10</u>
LucidDreamer [21] (w/ LoRA)	<u>48.45</u>	64.62	53.98	30.16	<u>57.31</u>	20.60	22.45	54.23	57.39	58.30	46.75
Ours	51.68	65.13	<u>47.23</u>	38.59	58.42	45.15	28.63	<u>57.12</u>	<u>57.55</u>	59.25	50.88

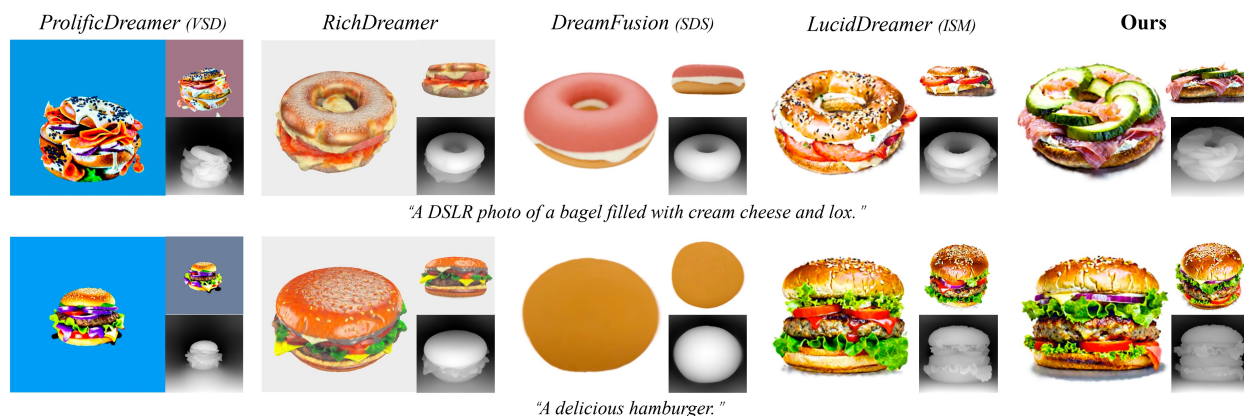


Figure 14. Qualitative comparison with state-of-the-art methods on natural scenes. Visual results demonstrate the superior performance of our approach.

- **Scalability:** Our distillation fusion (labeled "Addition" in the charts) consistently outperforms ablation fusion across all LoRA quantities, with performance advantages becoming more pronounced as complexity increases. Our method effectively handles multi-LoRA integration without suffering from interference effects that typically plague naive fusion strategies.
- **Stability:** The cosine similarity scores remain stable as the number of LoRAs increases, indicating robust fusion behavior. Unlike traditional methods that exhibit degradation with increased complexity, our approach maintains consistent performance even when integrating six different LoRAs.
- **Representational Coherence:** PCA analysis shows that our fusion maintains better alignment with the

original LoRA space. The geometric analysis reveals that our fusion strategy preserves essential directional characteristics while creating meaningful combinations, evidenced by tighter clustering patterns and reduced variance in principal components.

The cross-configuration analysis reveals our fusion method's performance advantage over ablation fusion becomes pronounced as the number of LoRAs increases. This suggests the benefits our approach are not merely additive, but are amplified when tackling complex, high-demand fusion scenarios. These quantitative findings, when combined with the comprehensive qualitative comparisons presented in Figure 10, provide strong evidence for the effectiveness and the superior generalizability of our proposed LoRA fusion strategy.



Q: These are the results generated by seven different text-to-3D methods with the prompt "A professional product photo of a precision hex <nut> with bright stainless steel surface, polished metallic finish, clean hexagonal edges.". Please rate the overall quality and details of the generated results from best to worst, and provide your reasons. Explain in a coherent paragraph.

A: Based on the visual quality, geometric accuracy, and surface detail of these text-to-3D generated hex nuts, I would rank them as follows from best to worst: **Image 7, Image 6, Image 5, Image 4, Image 3, Image 2, Image 1**. Image 7 demonstrates the highest quality with clean hexagonal geometry, convincing metallic surface rendering, and proper threading visible in the center hole—it closely resembles a professional product photograph. Image 6 follows closely with similar geometric precision and good surface reflections, though slightly less refined in the threading detail. Image 5 shows reasonable structural accuracy with visible threading, but the surface appears somewhat weathered or oxidized rather than the requested polished finish. Image 4 maintains basic hexagonal shape but lacks threading detail and presents a more matte, simplified appearance. Image 3 exhibits smooth geometry but completely omits the threaded hole, presenting instead as a simplified rounded hexagonal cap with poor adherence to the prompt. Image 2 shows severe geometric degradation with rough, artifact-laden surfaces that appear more like failed 3D printing than polished metal, though it attempts to show threading structure. Image 1 is clearly the worst, displaying catastrophic reconstruction failure with fragmented geometry, floating artifacts, and complete loss of structural coherence—it barely resembles a nut at all and suggests fundamental failure in the 3D generation pipeline.



(a) Nut



Q: These are the results generated by seven different text-to-3D methods with the prompt "A highly detailed, industrial-grade metallic <screw> with sharp helical threading and a polished steel surface.". Please rate the overall quality and details of the generated results from best to worst, and provide your reasons. Explain in a coherent paragraph.

A: Looking at these seven text-to-3D generation results, I would rank them from best to worst as follows: **Image 7, Image 3, Image 6, Image 5, Image 4, Image 2, Image 1**. Image 7 achieves the highest quality with exceptional geometric precision featuring a well-defined hexagonal socket head that demonstrates accurate internal drive geometry, clean and properly proportioned external threading on a short shaft, convincing stainless steel surface texture with appropriate metallic sheen, and effective lighting that highlights both the sharp edges and the fastener's overall form—it successfully represents a socket head cap screw (often called an Allen bolt) with professional-grade detail that closely matches the "bold, well-defined threading and crisp hexagonal head" specified in the prompt. Image 3 follows with good hexagonal head geometry, visible threading, and appropriate metallic finish, though the head design is simpler and the threading definition is slightly less refined than Image 7. Image 6 demonstrates solid construction with clear hexagonal features, well-rendered threading, and convincing steel appearance with blue-tinted highlights, though the shaft length exceeds the "short-shaft" specification. Image 5 shows recognizable fastener structure but exhibits an unusual faceted head appearance that deviates from standard hardware geometry, with less polished surface quality. Image 4 fundamentally misses the prompt by generating only a threaded cylindrical shaft without any hexagonal head component. Image 2 produces an amorphous, eroded form that barely resembles a fastener, lacking clear threading and geometric definition. Image 1 represents complete generation failure with chaotic, rainbow-colored fragmented geometry that bears no resemblance to any hardware component.



(b) Screw



Q: These are the results generated by seven different text-to-3D methods with the prompt "A professional close-up photograph of a clear <red_LED> with transparent dome-shaped epoxy casing and visible internal semiconductor chip". Please rate the overall quality and details of the generated results from best to worst, and provide your reasons. Explain in a coherent paragraph.

A: Looking at these seven text-to-3D generation results, I would rank them from best to worst as follows: **Image 7, Image 3, Image 5, Image 6, Image 4, Image 2, Image 1**. Image 7 achieves the highest quality with an accurate dome-shaped transparent red epoxy casing, properly rendered two-lead configuration, and visible internal structure that suggests the semiconductor chip—it successfully captures both the "clear" translucent quality and the characteristic LED form factor specified in the prompt. Image 3 follows closely with excellent dome geometry, appropriate translucency in the red casing, clearly defined leads, and reasonable internal detail visibility, though the surface appears slightly less refined than Image 7. Image 5 demonstrates good overall LED structure with proper dome shape and dual leads, but exhibits some surface artifacts and slight geometric irregularities that reduce the "professional close-up photograph" quality. Image 6 takes an interesting approach by attempting to show internal chip detail more explicitly, but the execution results in an overly complex, less accurate representation that doesn't maintain the characteristic smooth dome shape expected of an LED. Image 4 shows a simplified LED with reasonable proportions and red coloring, but lacks the transparent/translucent quality emphasized in the prompt and appears more opaque and toy-like rather than resembling a real electronic component. Image 2 fundamentally misinterprets the prompt by generating what appears to be a push-button or mechanical component with a red cap rather than an LED—it completely misses the dome-shaped epoxy casing and semiconductor nature. Image 1 represents total generation failure with fragmented, scattered geometry that bears no resemblance to an LED or any coherent 3D object, indicating complete inability to parse or execute the prompt.



(c) Red LED

Figure 15. LLM-based qualitative evaluation (Part 1-3).



Q: These are the results generated by seven different text-to-3D methods with the prompt "A professional close-up photograph of a clear <green_LED> with transparent dome-shaped epoxy casing and visible internal semiconductor chip. ". Please rate the overall quality and details of the generated results from best to worst, and provide your reasons. Explain in a coherent paragraph.

A: Looking at these seven text-to-3D generation results, I would rank them from best to worst as follows: **Image 7, Image 5, Image 3, Image 6, Image 4, Image 2, Image 1**. Image 7 achieves the highest quality with an exceptionally accurate dome-shaped transparent green epoxy casing, properly proportioned dual leads, visible internal structure suggesting the semiconductor chip, and the characteristic translucent quality that allows light to pass through—it perfectly captures the "clear" and "transparent" aspects emphasized in the prompt. Image 5 follows closely with excellent dome geometry, appropriate green translucency, well-defined leads, and visible internal details that suggest the chip structure, though the surface rendering is slightly less refined than Image 7. Image 3 demonstrates solid LED construction with good dome shape, proper transparency, and clear lead definition, successfully conveying the essential characteristics of a through-hole LED component, though with marginally less detail in the internal structure. Image 6 shows reasonable LED geometry and attempts to display internal chip detail more explicitly, but the addition of what appears to be a threaded base and overly complex internal structure makes it less accurate to a standard LED form factor, appearing more like a hybrid indicator light. Image 4 fundamentally misinterprets the prompt by generating what looks like a miniature light bulb with a screw base rather than an LED—while it has green coloring and transparency, it completely misses the characteristic LED dome shape and dual-lead configuration. Image 2 represents a significant deviation, producing what appears to be a multi-layered mechanical component or circuit board assembly rather than an LED, entirely missing the dome-shaped epoxy casing and simple two-lead structure. Image 1 shows complete generation failure with fragmented, chaotic geometry consisting of disconnected polygons and voxel-like artifacts that bear no resemblance to an LED or any coherent electronic component, indicating total inability to interpret the prompt.

(a) Green LED



Q: These are the results generated by seven different text-to-3D methods with the prompt "A detailed close-up photograph of a cylindrical <resistor> body only, with blue ceramic material and black color code bands around its surface. ". Please rate the overall quality and details of the generated results from best to worst, and provide your reasons. Explain in a coherent paragraph.

A: Looking at these seven text-to-3D generation results, I would rank them from best to worst as follows: **Image 7, Image 3, Image 5, Image 6, Image 4, Image 2, Image 1**. Image 7 achieves the highest quality with a clean cylindrical body, well-defined alternating blue and black color bands that accurately represent resistor color coding, proper proportions with axial leads, and smooth surface rendering that captures the ceramic material appearance specified in the prompt. Image 3 follows closely with excellent cylindrical geometry and clear band definition, showing good color separation between blue and black bands, though the overall form appears slightly more compressed than Image 7. Image 5 demonstrates similar quality to Image 3 with proper banding and cylindrical shape, but exhibits slightly more surface irregularities and less uniform band spacing that reduce the "detailed close-up photograph" quality. Image 6 shows reasonable resistor structure with blue coloring and visible leads, but the bands are less distinct and the body appears more like a solid blue cylinder with minimal color code detail, plus it includes text labeling that wasn't requested in the prompt. Image 4 presents a simplified interpretation with a predominantly blue cylindrical body but almost completely lacks the "black color code bands" that are central to the prompt, appearing more like a generic capacitor than a resistor. Image 2 fundamentally misinterprets the component by generating what appears to be a ribbed or corrugated cylindrical structure that looks more like a flexible connector or cable component rather than a resistor—while it has blue coloring, it completely misses the smooth ceramic body with distinct color bands. Image 1 represents total generation failure with chaotic, fragmented geometry showing disconnected polygons and artifacts that bear no resemblance to a cylindrical resistor or any coherent electronic component, indicating complete inability to parse the prompt.

(b) Resistor



Q: These are the results generated by seven different text-to-3D methods with the prompt "A photo of a great <bearing> ". Please rate the overall quality and details of the generated results from best to worst, and provide your reasons. Explain in a coherent paragraph.

A: Looking at these seven text-to-3D generation results, I would rank them from best to worst as follows: **Image 7, Image 3, Image 5, Image 6, Image 4, Image 2, Image 1**. Image 7 achieves the highest quality with a clean cylindrical body, well-defined alternating blue and black color bands that accurately represent resistor color coding, proper proportions with axial leads, and smooth surface rendering that captures the ceramic material appearance specified in the prompt. Image 3 follows closely with excellent cylindrical geometry and clear band definition, showing good color separation between blue and black bands, though the overall form appears slightly more compressed than Image 7. Image 5 demonstrates similar quality to Image 3 with proper banding and cylindrical shape, but exhibits slightly more surface irregularities and less uniform band spacing that reduce the "detailed close-up photograph" quality. Image 6 shows reasonable resistor structure with blue coloring and visible leads, but the bands are less distinct and the body appears more like a solid blue cylinder with minimal color code detail, plus it includes text labeling that wasn't requested in the prompt. Image 4 presents a simplified interpretation with a predominantly blue cylindrical body but almost completely lacks the "black color code bands" that are central to the prompt, appearing more like a generic capacitor than a resistor. Image 2 fundamentally misinterprets the component by generating what appears to be a ribbed or corrugated cylindrical structure that looks more like a flexible connector or cable component rather than a resistor—while it has blue coloring, it completely misses the smooth ceramic body with distinct color bands. Image 1 represents total generation failure with chaotic, fragmented geometry showing disconnected polygons and artifacts that bear no resemblance to a cylindrical resistor or any coherent electronic component, indicating complete inability to parse the prompt.

(c) Bearing

Figure 16. LLM-based qualitative evaluation (Part 4-6).



Q: These are the results generated by seven different text-to-3D methods with the prompt "A professional close-up photograph of a <ceramic_capacitor> with flat rectangular ceramic body and metallic end terminals. Precision electronic component with red ceramic dielectric material and silver terminations.". Please rate the overall quality and details of the generated results from best to worst, and provide your reasons. Explain in a coherent paragraph.

A: Looking at these seven text-to-3D generation results, I would rank them from best to worst as follows: **Image 4, Image 6, Image 3, Image 7, Image 5, Image 2, Image 1.** Image 4 achieves the highest quality with a proper rectangular ceramic body in red/pink coloring, clearly visible metallic threaded terminal at the base, appropriate proportions, and clean geometry that successfully represents a ceramic capacitor component, though it appears more like a larger power capacitor rather than a surface-mount type. Image 6 follows with reasonable component structure showing a red top section, visible metallic threading, dual leads, and an attempt at showing internal structure through transparency, though the execution makes it appear somewhat hybrid between different capacitor types. Image 3 demonstrates acceptable disc capacitor geometry with a red circular ceramic body and dual wire leads, representing a through-hole radial capacitor variant, though it deviates from the "flat rectangular" specification in the prompt by using a disc form factor. Image 7 shows similar disc capacitor structure with smoother surface rendering and appropriate red-brown ceramic coloring, but like Image 3, it misinterprets the rectangular body requirement while still capturing the essence of a ceramic capacitor. Image 5 exhibits a disc capacitor form with significant surface texture artifacts and irregular coloring that detracts from the "professional close-up photograph" quality, making it appear less like a precision electronic component. Image 2 fundamentally misinterprets the prompt by generating what appears to be a multi-unit array or module with stacked components, red separators, and yellow dots, completely missing the single discrete capacitor specification and looking more like a complex assembly than an individual component. Image 1 represents total generation failure with chaotic, fragmented geometry featuring iridescent rainbow coloring, scattered polygons, and completely incoherent structure that bears no resemblance to any type of capacitor, indicating complete inability to parse or execute the prompt successfully.

(a) Ceramic Capacitor



Q: These are the results generated by seven different text-to-3D methods with the prompt "A professional photograph of an ultra-thin flat <gasket>, circular shape with center hole, precision-engineered, stainless steel, industrial component, extremely thin profile, sharp details.". Please rate the overall quality and details of the generated results from best to worst, and provide your reasons. Explain in a coherent paragraph.

A: Looking at these seven text-to-3D generation results again, I would revise my ranking from best to worst as follows: **Image 3, Image 7, Image 2, Image 4, Image 5, Image 1, Image 6.** Image 3 achieves the highest quality with excellent circular geometry, a properly centered hole, convincing metallic surface texture suggesting stainless steel, and an appropriately ultra-thin profile clearly visible in the side view with sharp, clean edges conveying precision engineering. Image 7 follows with good circular form and appropriate thickness, though the surface appears more granular or textured, which could actually represent a realistic gasket material texture rather than being a flaw. Image 2 demonstrates solid gasket structure with a clean circular form and proper central hole, and the visible mounting holes around the perimeter are actually a realistic feature for industrial gaskets that need to be bolted in place, making this a legitimate interpretation despite not being explicitly mentioned in the prompt. Image 4 shows acceptable circular geometry with good flatness and appropriate proportions for a thin gasket, though the surface appears somewhat plain and less detailed. Image 5 exhibits reasonable gasket form with visible surface texture that could represent material grain or slight wear, though the texture appears somewhat excessive and the edges less precise. Image 1 is problematic because it shows a thick, yellow-tinted disc with significant discoloration that completely misses the "ultra-thin" and "stainless steel" specifications, appearing more like a plastic or composite material. Image 6 fundamentally misinterprets the prompt by generating a gear or sprocket with external teeth, which contradicts the basic "circular shape" specification for a simple flat gasket—this represents a completely different type of component regardless of its 3D modeling quality.

(b) Gasket



Q: These are the results generated by seven different text-to-3D methods with the prompt "A professional close-up photograph of a precision-manufactured <nail> with smooth cylindrical shank, flat circular head, and sharp tapered point. Polished steel construction with slight metallic sheen, high-quality hardware fastener. Studio lighting highlighting the metallic texture and form against neutral background.". Please rate the overall quality and details of the generated results from best to worst, and provide your reasons. Explain in a coherent paragraph.

A: Looking at these seven text-to-3D generation results, I would rank them from best to worst as follows: **Image 3, Image 7, Image 5, Image 2, Image 4, Image 6, Image 1.** Image 3 achieves the highest quality with accurate nail geometry featuring a properly proportioned flat circular head, smooth cylindrical shank, sharp tapered point, and convincing dark metallic finish that suggests polished steel with appropriate sheen—it successfully captures all the key elements specified in the prompt including the precision-manufactured appearance. Image 7 follows closely with excellent overall nail structure, clear flat head, cylindrical body, and pointed tip, along with good metallic rendering, though the surface texture shows slight irregularities that make it marginally less refined than Image 3. Image 5 demonstrates solid nail construction with appropriate proportions and visible metallic characteristics, but the head appears slightly more textured or worn and the overall surface quality is less polished than the top performers. Image 2 shows recognizable nail structure with a flat head and threaded/textured shank, but the spiral grooves and weathered appearance deviate from the "smooth cylindrical shank" and "polished steel" specifications, making it look more like a specialty fastener or aged hardware rather than a precision-manufactured standard nail. Image 4 fundamentally misinterprets the prompt by generating what appears to be a smooth, bullet-shaped or cosmetic applicator-like object that completely lacks the characteristic flat head of a nail, instead presenting an elongated teardrop form that doesn't represent hardware fastener geometry. Image 6 similarly produces an overly smooth, rounded form that looks more like a decorative or cosmetic item than a nail, with gradient coloring and lack of distinct head definition that fails to convey the utilitarian hardware nature specified. Image 1 represents complete generation failure with chaotic, fragmented geometry showing iridescent rainbow coloring and irregular polygonal forms that bear no resemblance to a nail whatsoever, indicating total inability to interpret or execute the prompt successfully.

(c) Nail

Figure 17. LLM-based qualitative evaluation (Part 7-9).



Q: These are the results generated by seven different text-to-3D methods with the prompt "A professional close-up of a short-shaft <nut_screw> with bold, well-defined threading and a crisp hexagonal head. Polished stainless steel surface under directional lighting reveals sharp edges and metallic texture.". Please rate the overall quality and details of the generated results from best to worst, and provide your reasons. Explain in a coherent paragraph.

A: Looking at these seven text-to-3D generation results, I would rank them from best to worst as follows: **Image 7, Image 3, Image 6, Image 5, Image 4, Image 2, Image 1.** Image 7 achieves the highest quality with exceptional geometric accuracy featuring a well-defined hexagonal head with crisp edges, clean and properly proportioned threading on a short shaft, convincing metallic surface texture suggesting polished stainless steel, and appropriate lighting that reveals the component's form—it successfully captures all essential characteristics of a precision fastener as specified in the prompt. Image 3 follows closely with accurate hexagonal head geometry, visible threading, reasonable proportions, and appropriate metallic finish, though the head appears slightly more rounded and the threading definition is marginally less sharp than Image 7. Image 6 demonstrates solid fastener construction with a clear hexagonal head, well-rendered threading, and good metallic appearance with blue-tinted highlights suggesting steel, though the shaft appears slightly longer than the "short-shaft" specification and some surface details are less refined. Image 5 shows recognizable bolt structure with hexagonal head and threading, but the head has an unusual faceted or crystalline appearance that deviates from typical hardware geometry, and the overall surface quality appears less polished despite attempting metallic rendering. Image 4 fundamentally misinterprets the prompt by generating what appears to be a set screw or threaded rod without any hexagonal head—it's essentially just a cylindrical threaded shaft, completely missing the "crisp hexagonal head" requirement that defines the fastener type. Image 2 significantly deviates by producing an amorphous, rock-like or eroded object with vague geometric features and minimal threading detail, appearing more like a weathered artifact than a precision-manufactured fastener, with only a hint of hexagonal form and no clear threading. Image 1 represents total generation failure with chaotic, fragmented geometry featuring iridescent rainbow coloring, scattered polygons, and completely incoherent structure that bears no resemblance to any hardware component, indicating complete inability to parse or execute the prompt successfully.



(a) Hexagonal Stud



Q: Please use a short paragraph to evaluate the overall effectiveness of these seven models and rank them.

A: Based on the comprehensive evaluation across nine different industrial component prompts (hex nut, screw, red LED, green LED, resistor, bearing, ceramic capacitor, gasket, nail, and nut-screw), a clear performance hierarchy emerges among these seven text-to-3D generation methods. Overall ranking from best to worst: **Model 7, Model 3, Model 6, Model 5, Model 4, Model 2, Model 1.** Model 7 demonstrates exceptional consistency and reliability, consistently producing geometrically accurate results with proper material rendering, clean edges, and faithful adherence to prompt specifications—it excels particularly at precision components requiring sharp detail and metallic finishes. Model 3 follows as a strong performer with good geometric accuracy and reasonable surface quality, though occasionally showing simplified details or less refined textures compared to Model 7. Model 6 shows decent competency with recognizable component structures and appropriate material rendering, but sometimes introduces unnecessary complexity or deviates from standard component forms. Model 5 produces variable results with acceptable basic geometry but frequently exhibits surface artifacts, crystalline appearances, or texture irregularities that reduce realism. Model 4 demonstrates significant weaknesses by often misinterpreting fundamental component characteristics—generating wrong geometries like threaded rods instead of headed fasteners or bullet shapes instead of nails—despite occasionally showing clean surface rendering. Model 2 consistently struggles with accuracy, frequently producing oversimplified, weathered, or completely wrong component types (like mechanical assemblies instead of simple capacitors), indicating poor prompt comprehension. Model 1 represents catastrophic failure across nearly all prompts, generating fragmented, chaotic geometry with rainbow artifacts and scattered polygons that bear no resemblance to the requested objects, suggesting fundamental issues in the generation pipeline that prevent any useful output.



(b) Overall Comment

Figure 18. LLM-based qualitative evaluation (Part 10-11).